High-Fidelity Simulations of a Quadrotor Vehicle for Urban Air Mobility

Patricia Ventura Diaz* and Seokkwan Yoon†
NASA Ames Research Center, Moffett Field, CA, 94035

High-fidelity computational fluid dynamics simulations have been carried out to analyze NASA's quadrotor air taxi concept for urban air mobility. High-order accurate schemes, dual-time stepping, and the delayed detached-eddy simulation model have been employed. The flow solver has been loosely coupled with the rotorcraft comprehensive analysis code. The vehicle simulated is a six-passenger quadrotor for air taxi operations. The quadrotor has been simulated in hover and cruise, with flight conditions representative of an air taxi mission. Initially, the quadcopter vehicle is analyzed using low-fidelity tools. Then, a complete analysis using high-fidelity simulations of the quadcopter is performed in conjunction with collective pitch control. Airloads, wake geometry, and performance are studied and compared. A comparison between isolated rotors and complete vehicle simulations is presented. NASA's quadrotor is one of NASA's concept vehicles designed in support of aircraft development for vertical take-off and landing air taxi operations.

Nomenclature

T	Rotor thrust
P	Rotor power
Q	Rotor torque
C_T	Thrust coefficient, $\frac{T}{\rho A(\Omega R)^2}$
C_P	Power coefficient, $\frac{P}{\rho A(\Omega R)^3}$
C_Q	Torque coefficient, $\frac{Q}{\rho A(\Omega R)^2 R}$
C'	Sectional chord force
N'	Sectional blade normal force
M'	Sectional blade pitching moment
M^2c_c	Sectional chord force coefficient, $\frac{C'}{\frac{1}{2}\rho a^2 c}$
M^2c_n	Sectional normal force coefficient, $\frac{N'}{\frac{1}{2}\rho a^2 c}$
M^2c_m	Sectional pitching moment coefficient, $\frac{M'}{\frac{1}{2}\rho a^2 c^2}$
M	Mach number, $\frac{V}{a}$
M_{tip}	Mach number at the blade tip, $\frac{\Omega R}{a}$
Re	Reynolds number, $\frac{VL_{\text{ref}}}{\nu}$
Re_{tip}	Reynolds number at the blade tip, $\frac{\Omega R c_{\text{tip}}}{\nu}$
a	Fluid speed of sound
d	Turbulent length scale
y^+	Non-dimensional viscous wall spacing
A	Rotor disk area
R	Rotor radius
W	Weight
r	Radial position
c	Local rotor blade chord length
V_∞	Freestream velocity
α	Angle of Attack (AoA)
β_0	Coning angle
β_{1c}	Longitudinal flapping angle
β_{1s}	Lateral flapping angle
θ_0	Collective angle
θ_{1c}	Lateral cyclic pitch
θ_{1s}	Longitudinal cyclic pitch
ψ	Azimuth position
δ	Boundary layer thickness
μ	Advance ratio, $\frac{V_\infty \cos\alpha}{\Omega R}$
σ	Rotor solidity
ν	Fluid kinematic viscosity
ρ	Fluid density
Δ	Grid spacing
Ω	Rotor rotational speed

Subscript

front	Front rotor
rear	Rear rotor
root	Blade root
tip	Blade tip
∞	Freestream

*Research Scientist, STC, Computational Physics Branch, Member AIAA.
†Chief, Computational Physics Branch.

I. Introduction

Urban Air Mobility (UAM) vehicles are conceived to be the future means of transportation in urban areas. Air taxis are being designed with single- or multi-rotor configurations, which allow them for Vertical Take-Off and Landing (VTOL) operations. With air taxis, travel times may be drastically reduced in highly congested cities by avoiding ground traffic. Relying on either hybrid or electric propulsion systems, UAM vehicles will provide a greener means of transportation.

The NASA Revolutionary Vertical Lift Technology (RVLT) project has been developing tools and datasets to support the design of advanced vertical lift aircraft. RVLT is designing several UAM concept vehicles, with the objective to focus and guide the research activities in support of aircraft development for emerging aviation markets. The concept vehicles include quadrotor, side-by-side aircraft, quiet single-main rotor helicopter, lift+cruise aircraft, and tiltwing aircraft configurations [1].

Fig. 1 NASA's quadrotor UAM concept.

NASA's quadrotor, shown in Figure 1, is intended to represent multi-rotor UAM aircraft configurations and will be the focus of this work. The quadcopter uses collective control for flight control. The mission is common to all NASA UAM concept vehicles (quadrotor, side-by-side, lift+cruise, tiltwing, etc.) and consists of: two 37.5 nm flights without recharging or refueling, with a 20 min reserve, carrying six passengers (including the pilot if not autonomous). All NASA concept vehicles have been designed to perform this mission. Johnson *et al.* [1] summarize NASA's UAM design tools, missions, and vehicle concepts.

The quadrotor concept has been designed with the rear rotors mounted higher on the aircraft than the front rotors. Initial free wake comprehensive analysis during the design phase observed that the rotor power required for cruise was significantly reduced [2]. High-fidelity Computational Fluid Dynamics (CFD) analysis later confirmed the benefits of reducing the rotor-rotor interactions by mounting the rear rotors higher than the front rotors [3]. This phenomenon was first studied by Ventura Diaz *et al.* [4] for small quadcopters drones.

The accurate prediction of rotorcraft performance and acoustics is challenging from a computational point of view because the flows are unsteady, nonlinear, and complex. In the case of multi-rotor vehicles, the aerodynamic interactions between the rotors (and other components when simulating the complete vehicle) make the problem even more difficult. While low-fidelity tools offer the advantage of a short turn-around and low computational cost, only high-fidelity methods can capture the complex flow details and the aerodynamic interactions. In addition, high-fidelity simulations can provide the information needed to calibrate the lower fidelity tools that can be used for design purposes.

Previous high-fidelity CFD work performed by Ventura Diaz *et al.* [3–8] and Yoon *et al.* [9] includes simulations of NASA's quadrotor isolated rotors [3], NASA's side-by-side air taxi concept [5, 6], ducted and coaxial rotors [7], and computational analysis of small multi-rotor vehicles [4, 8, 9].

The objectives of the present work are to simulate and analyze NASA's quadrotor UAM concept using high-fidelity CFD. The quadrotor vehicle will be analyzed in different flow conditions and compared to previous work that showed the results for the isolated rotors or "rotors-only" configuration [3]. The quadrotor simulations using high-fidelity CFD are loosely coupled with a comprehensive rotorcraft code for accurate prediction of blade motions and airloads. The rotor wake geometry, airloads, and performance are analyzed for each case.

Although there are no validation data for these simulations, the computational data might be valuable for future validation testing.

II. Numerical Approach

The flow solver used in this study is NASA's OVERFLOW [10] CFD solver. OVERFLOW is a finite-difference, structured overset grid, high-order accurate Navier-Stokes flow solver. NASA's Chimera Grid Tools (CGT) [11] overset grid generation software is used for generating the overset grids of rotors and complete vehicles. Body-fitted curvilinear Near-Body (NB) grids are generated using CGT. The computational domain is completed with the generation of Cartesian Off-Body (OB) grids that are automatically generated prior to grid assembly using the domain connectivity framework in OVERFLOW-D mode. The current time-accurate approach consists of an inertial coordinate system where NB curvilinear O-grids for the rotor blades rotate through the fixed OB Cartesian grid system. Overflow is loosely coupled with the helicopter comprehensive code CAMRAD II [12]. The CFD provides high-fidelity, nonlinear aerodynamics that replace the comprehensive lifting line aerodynamic analysis from CAMRAD II. The comprehensive code performs the structural dynamics and trim calculations and gives the information to OVERFLOW. The loose coupling allows for a modular approach and communication through input/output. The coupling methodology has been implemented following the approach of Potsdam *et al.* [13].

The numerical approach and the coupling process are described in the following paragraphs.

A. Overset Grid Generation

The overset grid generation process using CGT can be divided into the following steps: geometry processing, surface grid generation, volume grid generation, and domain connectivity [11].

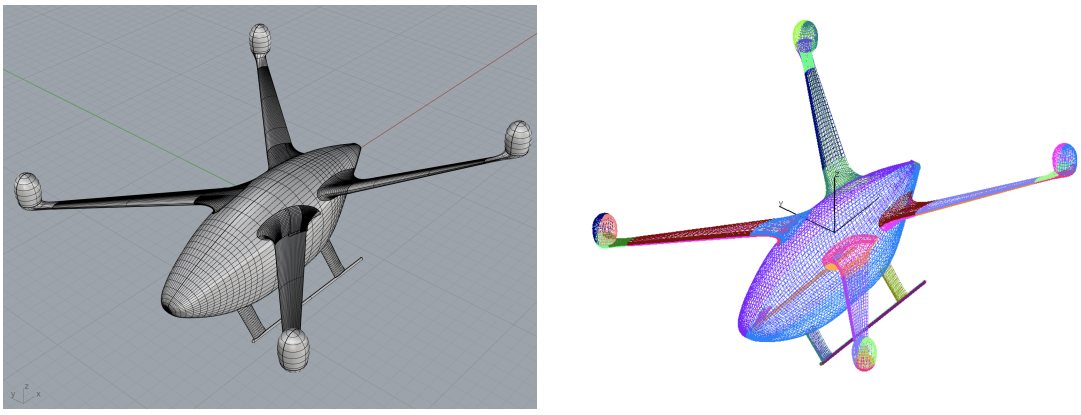

(a) CAD geometry **(b) EGADS output**

Fig. 2 The quadrotor air taxi airframe. Figure 2a shows the CAD geometry. In Figure 2b, the structured untrimmed patches obtained from the CAD geometry using EGADS are depicted. The patches are used as reference surfaces to generate the overset surface grids.

The geometry is usually obtained from a Computer-Aided Design (CAD) model. The Boundary Representation (BRep) is an object that holds both the topological entities and the geometric components [14]. In this work, a pre-processing step converts the analytical BRep solid from a STEP or IGES file into discrete representations for the BRep faces and edges. Access to the model topology and entities is accomplished through EGADS (Engineering Geometry Aerospace Design System) API, a foundational component of the Engineering Sketch Pad [14]. With the *egads2srf* tool, discrete representations are generated from each solid. Figure 2 shows the structured surface grid file obtained using EGADS. This grid file contains an untrimmed structured patch for each face based on the tessellation of the face parameter space. Another file obtained with *egads2srf* is a curve grid file containing tessellated edges. The curve grid file and the structured grid file from EGADS are then used as an input for the overset surface grid generation step.

Overset structured surface grids are typically created using a combination of algebraic and hyperbolic methods, depending on the number of initial curves on each surface domain and the topology of the region of interest. The generation of surface grids is the step that requires the most manual effort and experience from the user. Figure 3 shows the overset surface grids for the quadrotor. The complete vehicle consists of the rotors, hubs, hub supports, wings, landing gear, and main airframe.

With sufficient overlap between surface grids, the volume grids can be created easily with hyperbolic marching

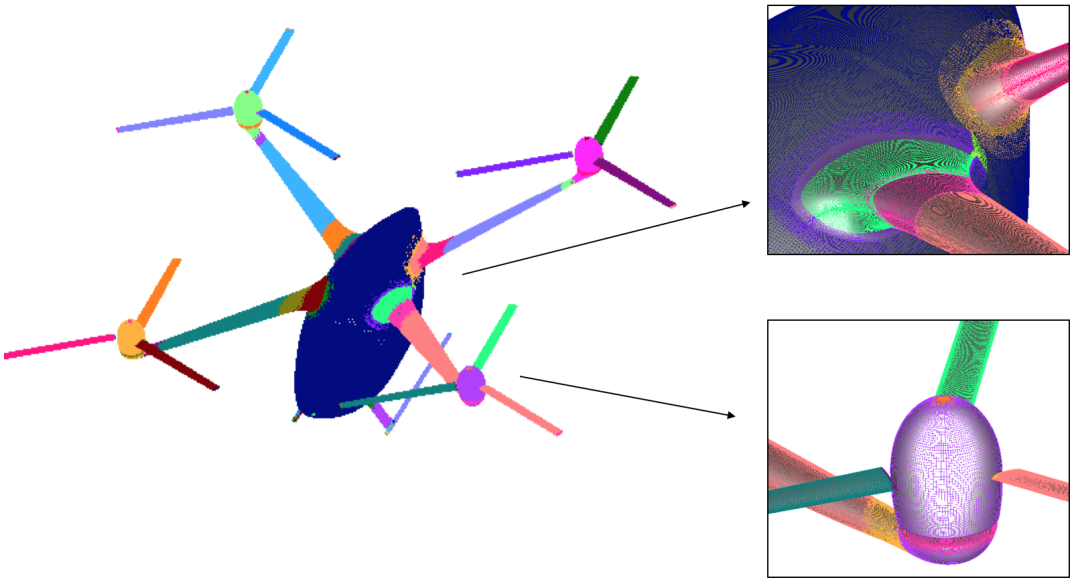

Fig. 3 Quadrotor overset surface grids. The left image shows the complete vehicle, including the rotors. The top right image shows the junctions of the wings with the fuselage in detail. The bottom right image shows the hub and hub support.

methods out to a fixed distance from the surface. Such methods provide orthogonal grids with tight clustering characteristics near the wall, which is essential for accurately capturing the boundary layer in viscous flow computations. The distance is chosen such that the outer boundaries of the NB volume grids are well clear off the boundary layer. The NB grids are then embedded inside OB Cartesian grids that extend to the far-field.

OB Cartesian grids with uniform spacing surround the NB grids to resolve the wake region of interest. Coarser Cartesian grids efficiently expand the grid system to the far-field, where each successive Cartesian grid is twice as coarse as its previous neighbor. The far-field boundary is 20 rotor radii away from the center of the vehicle in all directions. The resolved wake region has a uniform grid spacing of 10% of the tip chord length, c_{tip}.

The rotor geometry information from Table 1 has been used to generate the blade grids. The profiles used to build the blade are 10.6% thick modern airfoils from $r = 0$ to $r = 0.85R$, and 9% thick modern airfoils from $r = 0.95R$ to the tip $r = R$. The transition between the two different airfoil sections is smooth (linear interpolation with the radial stations). The blade is tapered near the tip. Figure 4 shows in detail the quadrotor vehicle blade grids. Surface grid resolution on the rotor blades is clustered in the chordwise direction near the airfoils leading and trailing edges to resolve large pressure gradients accurately. Subsequently, the spanwise resolution is clustered near the root and the tip. The normal grid spacing of all grids at the walls maintains $y^+ \leq 1$.

Table 1 Quadrotor rotor geometry properties.

Properties	Values
Number of rotors	4
Number of blades/rotor	3
Radius, R	2.809 m
Linear twist	-12 deg
Root chord, c_{root}	0.217 m
Tip chord, c_{tip}	0.176 m
Rotor solidity, σ	0.0647
Nominal tip speed, V_{tip}	167.6 m/s

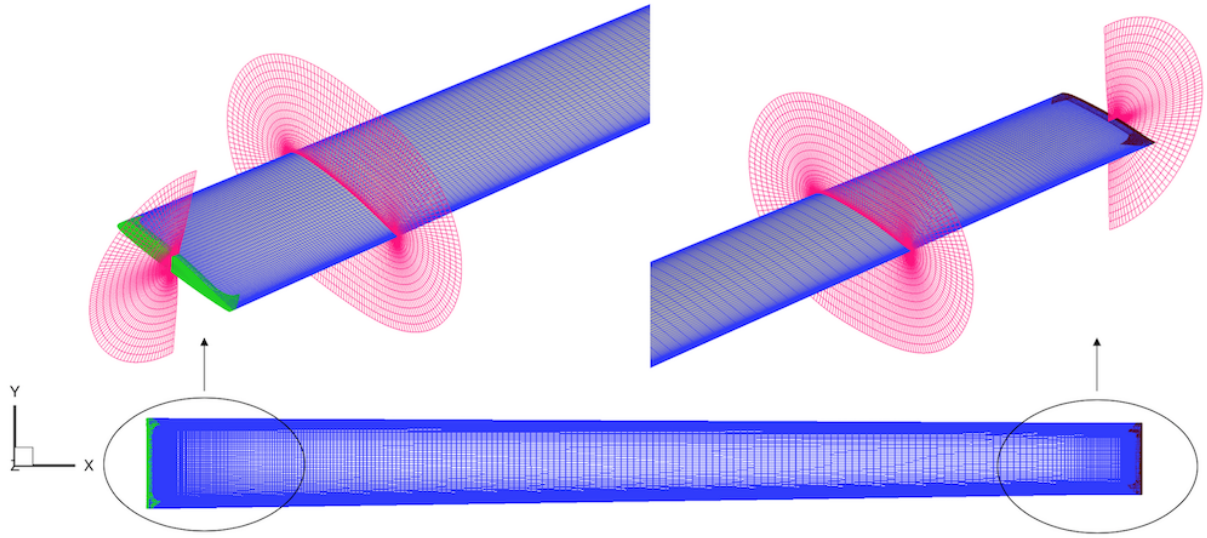

Fig. 4 Blade overset grids for the quadrotor urban air taxi. The NB root and tip grids are shown in detail. Cap grids are used for the root (green) and tip (brown), O-grids are used for the blade (blue). Slices of the volume grids are shown in magenta. There is clustering near the leading edge, trailing edge, blade tip, and blade root, to resolve the large pressure gradients near these regions.

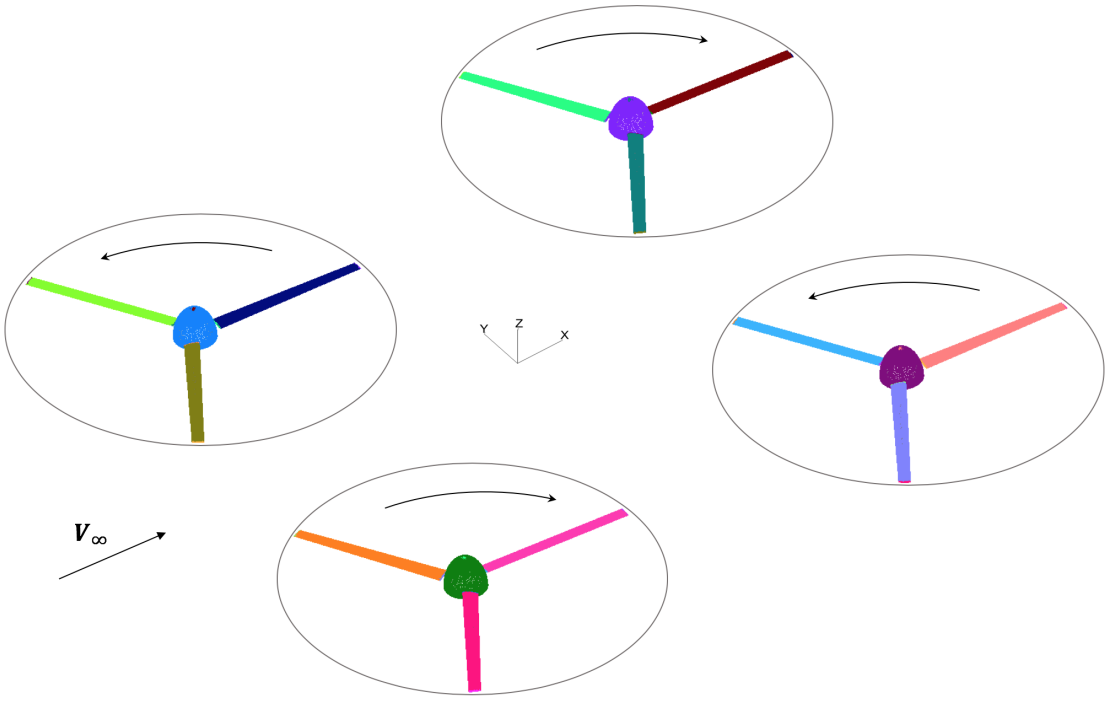

Fig. 5 Quadrotor rotors-only overset surface grids. The image illustrates the direction of rotation of each individual rotor.

The multi-rotor system consists of four rotors, with three blades per rotor. The right front rotor (rotor 1) rotates counter-clockwise (CCW), the left front rotor (rotor 2) rotates clockwise (CW), the right rear rotor (rotor 3) rotates CW, and the left rear rotor (rotor 4) rotates CCW. Therefore the advancing blade is outboard for the front rotors, and inboard for the rear rotors. The rotor grids without airframe are shown in Figure 5. A -3° alpha shaft angle is included for all the rotors. The locations of each rotor are summarized in Table 2. Johnson and Silva [2] obtained this final configuration of the quadcopter using Multidisciplinary Design, Analysis, and Optimization (MDAO) tools, for which the power required to cruise is reduced by decreasing the interference of the wakes of the front rotors on the rear rotors. In addition, "moving the aircraft center of gravity forward of the mid-point between the rotors, so the front and the rear rotors trim closer to the same C_T/σ at cruise speed, further reduces the power", they explained. Ventura Diaz *et al.* [3] conducted a high-fidelity computational analysis of the quadrotor rotors without airframe. In cruise, a rotor power reduction of 8% for the final configuration compared to the initial rotor placement without vertical separation was observed, verifying the initial findings from Johnson and Silva.

Table 2 Rotor placement of quadcopter vehicle.

Rotor Number	Rotation	x	y	z
Rotor 1	CCW	$-1.35R$	$1.35R$	$0.25R$
Rotor 2	CW	$-1.35R$	$-1.35R$	$0.25R$
Rotor 3	CW	$1.35R$	$1.35R$	$0.6R$
Rotor 4	CCW	$1.35R$	$-1.35R$	$0.6R$

By using a trimmed approach, the domain connectivity step is robust and highly automated: hole cutting is required between components and with the OB Cartesian grids. In this study, the X-ray hole cutting method is used. An X-ray object is created for every component in the geometry (i.e., the blades, the hubs, the fuselage, the landing gear, etc.). The user has to supply the list of meshes that each X-ray object is allowed to cut and an offset distance with which to grow each hole away from the body. The hole cutting process is performed at each time step within the flow solver, allowing for the rotation of the blades relative to the fixed components.

The number of grids and grid points for the configurations studied is presented in Table 3.

Table 3 NB and OB grid features of all configurations studied.

Configuration	NB grids	NB grid points	NB+OB grid points hover	NB+OB grid points cruise
Only-rotors	48	57×10^6	312×10^6	301×10^6
Complete vehicle	122	105×10^6	440×10^6	434×10^6

B. High-Order Accurate Navier-Stokes Solver

The Navier-Stokes equations can be solved using finite differences with a variety of numerical algorithms and turbulence models. The time-dependent Reynolds-Averaged Navier-Stokes (RANS) equations are solved in strong conservation form:

$$\frac{\partial \boldsymbol{q}}{\partial t} + \frac{\partial (\boldsymbol{F} - \boldsymbol{F}_\mathrm{v})}{\partial x} + \frac{\partial (\boldsymbol{G} - \boldsymbol{G}_\mathrm{v})}{\partial y} + \frac{\partial (\boldsymbol{H} - \boldsymbol{H}_\mathrm{v})}{\partial z} = 0, \tag{1}$$

being $\boldsymbol{q} = [\rho, \rho u, \rho v, \rho w, e]^\intercal$ the vector of conserved variables; $\boldsymbol{F}$, $\boldsymbol{G}$ and $\boldsymbol{H}$ the inviscid flux vectors; and $\boldsymbol{F}_\mathrm{v}$, $\boldsymbol{G}_\mathrm{v}$ and $\boldsymbol{H}_\mathrm{v}$ the viscous flux vectors.

In this study, the diagonal central difference algorithm is used with the 5^{th}-order accurate spatial differencing option with scalar dissipation. The physical time step corresponds to 0.25 degrees rotor rotation, together with up to 50 dual-time sub-iterations for a 2.5 to 3.0 orders of magnitude drop in sub-iteration residual. The numerical approach and time step were previously validated for various rotor flows [15–17].

C. Hybrid Turbulence Modeling

The OVERFLOW code has a choice of algebraic, one-equation, and two-equation turbulence models, including hybrid Reynolds-Averaged Navier-Stokes / Large Eddy Simulation (RANS/LES) models that close the RANS equations. In this study, the one equation Spalart-Allmaras [18] turbulence model is used primarily within the boundary layer.

The intent of the Detached Eddy Simulation (DES) model [18] is to be in RANS mode throughout the boundary layer, where the turbulent scales can be very small and need to be modeled, and in LES mode outside the boundary layer where the largest turbulent scales are grid-resolved. In this way, DES is a RANS/LES hybrid approach that mitigates the problem of artificially large eddy viscosity. The turbulence length scale d is replaced by $\overline{d}$, where $\overline{d}$ is the minimum of the distance from the wall d and the local grid spacing times a coefficient.

The DES approach assumes that the wall-parallel grid spacing $\Delta_{\parallel}$ exceeds the thickness of the boundary layer δ so that the RANS model remains active near solid surfaces. If the wall-parallel grid spacing is smaller than the boundary layer thickness $\Delta_{\parallel} < \delta$, then the DES Reynolds stresses can become under-resolved within the boundary layer; this may lead to non-physical results, including grid-induced separation. Using Delayed Detached Eddy Simulation (DDES) [19], the RANS mode is prolonged and is fully active within the boundary layer. The wall-parallel grid spacing used in this study does not violate the hybrid-LES validity condition; thus DES and DDES should give similar results. Nevertheless, all computations have been performed using the DDES model for both NB and OB grids.

D. Comprehensive Analysis

CAMRAD II [12, 20] is a comprehensive analysis code of rotorcraft; it simultaneously solves the rotor dynamics and aerodynamics for a trimmed or transient flight condition. CAMRAD II incorporates a combination of advanced technologies, including multibody dynamics, nonlinear finite elements, and rotorcraft aerodynamics. The trim task finds the equilibrium solution for a steady-state operating condition and produces the solution for performance, loads, and vibration. The aerodynamic model for the rotor blade is based on lifting-line theory, using two-dimensional airfoil characteristics and a vortex wake model. CAMRAD II has undergone extensive correlation with performance and loads measurements on rotorcraft.

Structural dynamics, vehicle trim, and rotor trim for the coupled CFD calculations are performed using the comprehensive rotorcraft analysis code CAMRAD II.

E. Loose Coupling OVERFLOW – CAMRAD II

A loose coupling approach between OVERFLOW and CAMRAD II based on a trimmed periodic rotor solution is implemented. The comprehensive code provides the trim solution and blade kinematic and elastic motions. The high-fidelity CFD calculates the airloads. Figure 6 shows the flow diagram of the loose coupling strategy. In summary, the CFD airloads replace the comprehensive airloads while using lifting line aerodynamics to trim and computational structural dynamics to account for blade deformations.

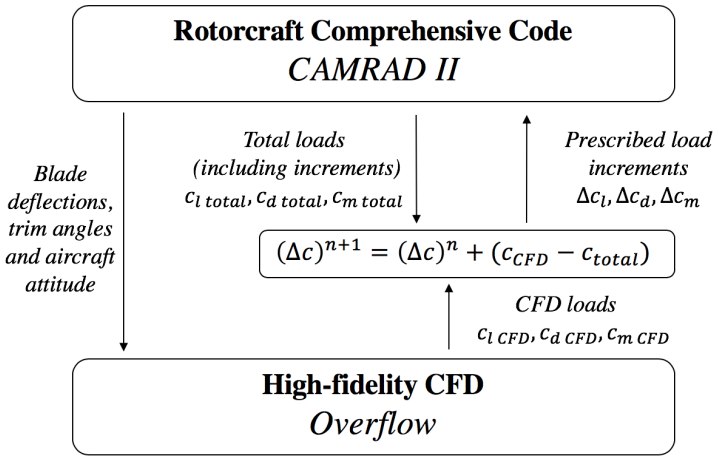

Fig. 6 Flow diagram for CFD/Comprehensive Analysis loose coupling methodology.

The iterative loose coupling process is summarized next. The simulation is initialized with a comprehensive analysis resulting in a trimmed rotor solution obtained with lifting line aerodynamics and uniform inflow. This analysis creates initial quarter chord motions as a function of the radius r and the azimuth ψ, for each rotor. In addition, the aircraft attitude is also obtained from CAMRAD II. The motions and aircraft pitch angle are given to the CFD. The CFD analysis accounts for the entire flow field, and therefore it only requires the structural motion. The CFD is run with the prescribed motions and angles, for two to five full rotor revolutions for the first coupling step. OVERFLOW outputs the normal force N', pitching moment M', and chord force C' as a function of radius and azimuth.

Then, the aerodynamic force and moment coefficients increments (Δc) that are used in the comprehensive code at the next iteration $n+1$ are calculated. The increments are the difference between the CFD loads and the comprehensive lifting line solution required to trim from the previous step n, plus the load increments from the previous step:

$$(\Delta c)^{n+1} = (\Delta c)^n + (c_{\text{CFD}} - c_{\text{total}}) \tag{2}$$

For the initial step, the increments are the difference between CFD and the total loads from the 0^{th} run in CAMRAD II:

$$(\Delta c)^1 = (c_{\text{CFD}} - c_{\text{total}})$$

The sectional pitching moment $M^2 c_m$, normal force $M^2 c_n$ and chord force $M^2 c_c$ coefficients are defined as:

$$M^2 c_m = \frac{M'}{\frac{1}{2}\rho a^2 c^2} \tag{3}$$

$$M^2 c_n = \frac{N'}{\frac{1}{2}\rho a^2 c} \tag{4}$$

$$M^2 c_c = \frac{C'}{\frac{1}{2}\rho a^2 c} \tag{5}$$

The CFD is rerun with the new quarter chord motions of the retrimmed rotor and the new aircraft attitude. The previous CFD flow solution is used as restart condition. The coupling is performed every half or quarter rotor revolution. The coupling solution is considered to be converged when collective and cyclic control angles and the CFD airloads do not change between iterations. The CFD flow solution is usually converged after 10 to 20 rotor revolutions.

The coupling procedure is valid as long as the rotor loads are periodic. This approach is still good if there is some aperiodicity in the vortex wake, which is often the case in high-resolution turbulent simulations.

III. Free Wake Results

Thi section presents an initial study using the free wake analysis with the rotorcraft comprehensive code CAMRAD II for the quadrotor. In multi-rotor configurations, a free convecting wake is required in order to predict the performance accurately. In addition, blade-vortex interaction airloads are important to capture for noise calculations. First incorporated into the code in 1994 [21], CAMRAD II free wake model has been validated extensively over the years.

The flight conditions are summarized in Table 4, which are representative of a UAM mission. In cruise, the freestream velocity is $V_\infty = 121.64$ kts, with an advance ratio of $\mu = 0.373$.

Table 4 Flight conditions for the quadrotor urban air taxi simulations.

h	T_∞	Ω	V_{tip}	M_{tip}	V_∞	M_∞	Re
5000 ft	ISA +20^{o}C	59.685 rad/s	550 ft/s	0.484	121.6 kts	0.181	1.7×10^6

The quadrotor vehicle in this study is designed with collective control. A version of the same vehicle with RPM control has also been designed but will not be the focus of this work. A comparison of the trim and performance between collective and RPM control was done in [2].

CAMRAD II free wake simulations are run on a single processor. Figure 7 shows the rotor wake geometries in hover and cruise flow conditions. CAMRAD II has been set up such that the rotors are allowed to interact aerodynamically: at

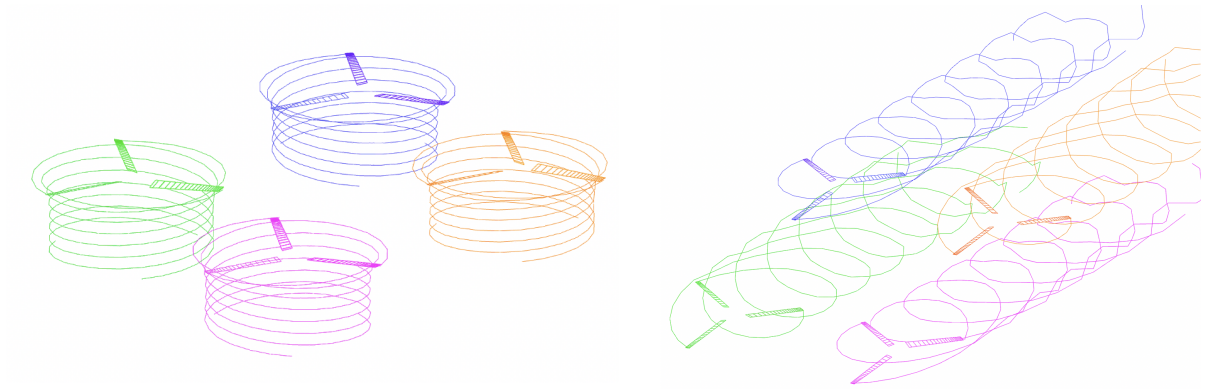

(a) Hover **(b) Cruise**

Fig. 7 Quadrotor wake geometry in hover (Fig. 7a) and cruise (Fig. 7b) obtained using CAMRAD II free wake simulations. Rotor 1 (front-right rotor) and its wake are shown in green, rotor 2 (front-left rotor) is shown in magenta, rotor 3 (rear-right rotor) is shown in blue, and rotor 4 (rear-left rotor) is shown in orange.

each analysis point the aerodynamics on one rotor is influenced by the non-uniform induced velocities from the other rotors. The wakes are plotted for three rotor revolutions.

The flapping and collective angles in hover and in cruise are shown in Tables 5 and 6, respectively. The solution is symmetric between left and right components. There is almost no flapping in hover ($\beta_{1c} \approx 0$, $\beta_{1s} \approx 0$). Front rotors trim to a higher collective θ_0. In cruise, coning angles (β_0) are almost the same between front and rear rotors and collectives are higher for the rear rotors.

Table 5 Final angles for the quadrotor in hover conditions, using CAMRAD II free wake analysis.

Rotor number	β_0 [^{o}]	β_{1c} [^{o}]	β_{1s} [^{o}]	θ_0 [^{o}]
Rotor 1	2.78	0.07	-0.01	11.67
Rotor 2	2.78	0.07	-0.01	11.67
Rotor 3	2.43	-0.05	0.01	10.281
Rotor 4	2.43	-0.05	0.01	10.281

Table 6 Final angles for the quadrotor in cruise conditions, using CAMRAD II free wake analysis.

Rotor number	β_0 [^{o}]	β_{1c} [^{o}]	β_{1s} [^{o}]	θ_0 [^{o}]
Rotor 1	2.36	-4.54	3.53	12.43
Rotor 2	2.36	-4.54	3.53	12.43
Rotor 3	2.37	-4.65	3.67	12.77
Rotor 4	2.37	-4.65	3.67	12.77

The hover efficiency is measured in terms of the figure of merit, which is the ratio between the ideal power and the actual power required to hover. The vehicle figure of merit is $FM = 0.799$, and the figure of merit for the front rotors and rear rotors are: $FM_{\text{front}} = 0.77$ and $FM_{\text{rear}} = 0.762$. A slightly smaller FM is found for the rear rotors as they are operating at smaller collective. This is due to the vehicle trim and the location of the center of gravity. The rear rotors are placed higher along the vertical axis, and the vehicle center of gravity is located at $(x, y, z) = (-0.244, 0, 0)$ m.

The cruise efficiency is measured by the effective lift-to-drag L/D_{e} ratio. The aircraft and rotor lift-to-drag ratio are

defined as:

$$\frac{L}{D_{\mathrm{e}}} = \frac{WV_{\infty}}{P} \tag{6}$$

$$\frac{L}{D_{\mathrm{e}}} = \frac{LV_{\infty}}{P_0 + P_i} \tag{7}$$

L/D_e is an appropriate measure of edgewise efficiency. For the quadrotor, the aircraft L/D_{e} is 5.135. The lift-to-drag ratio of the front rotors is $L/D_{\mathrm{e}} = 8.913$, and for the rear rotors is $L/D_{\mathrm{e}} = 7.996$. The rear rotors are relatively less efficient than the front rotors.

IV. High-Fidelity CFD Results

In this section, the loosely-coupled CAMRAD II-OVERFLOW results will be presented. The comparison between the rotors-only (see Fig. 5) and complete vehicle (see Fig. 3) configurations in hover and in cruise will be done in this section. The flight conditions are the same as for the free wake analysis, as shown in Table 4.

All simulations have been run using NASA's supercomputers Pleiades, Electra, and Aitken located at the NASA Advanced Supercomputing (NAS) Division, utilizing 2000 processors.

The approach follows the loose coupling methodology between CAMRAD II and OVERFLOW, as depicted in Section II.E. For the loose coupling, CAMRAD II needs only to be run using uniform inflow (instead of free wake). As the aerodynamics will be replaced by the CFD solution, uniform inflow is enough to run CAMRAD II, allowing for much faster CAMRAD II solutions and overall coupling simulations time performance.

A. Hover

Hover simulations were run using NASA's supercomputers with 2080 processors on Skylake and Rome nodes, for 10 days. At the end of the simulation, the rotors had rotated 27 revolutions.

The rotor thrust and torque coefficients are presented in Figures 8 and 9, calculated from the OVERFLOW solution. The C_T and C_Q are calculated for each rotor and each rotor blade. Periodic peaks on the thrust coefficient evolution are observed, with a period of 1 revolution. The frequency on the total thrust of each rotor for the peaks is $\frac{1}{3\mathrm{rev}}$. Note that a revolution is equivalent to 1440 iterations. The torque of each blade follows a smooth distribution. As rotors 2 and 3 rotate clock-wise, the sign for C_Q is opposite to that of CCW rotors. It can be observed that the CFD solution is converged as the aerodynamic coefficients are periodic. Small differences between periods are normal and are due to the unsteady behavior of a turbulent flow.

The Overflow - CAMRAD II loose coupling approach is considered converged when the delta airloads differences between one iteration to the next are very small. This is also reflected on the trim angles evolution with the coupling step. Figure 10 shows the coning angle β_0, the flapping angles β_{1c} and β_{1s}, and the collective pitch angle θ_0 for the four rotors. After approximately 10 iterations, the change in trim angles is relatively small, and thus the coupling approach can be considered to be converged.

Table 7 Final angles for the quadrotor rotors-only and complete vehicle configurations, in hover conditions.

Configuration	Rotors-only				Complete Vehicle			
Rotor # / Angles	β_0 [^{o}]	β_{1c} [^{o}]	β_{1s} [^{o}]	θ_0 [^{o}]	β_0 [^{o}]	β_{1c} [^{o}]	β_{1s} [^{o}]	θ_0 [^{o}]
Rotor 1	2.74	-0.39	0.21	12.72	2.71	-0.44	0.29	11.02
Rotor 2	2.73	-0.38	0.22	12.70	2.61	-0.35	0.11	12.17
Rotor 3	2.38	0.48	-0.29	11.36	2.21	0.31	-0.20	10.02
Rotor 4	2.38	0.48	-0.30	11.37	2.48	0.37	-0.16	11.72

A comparison of the final coning, flapping, and collective angles for each rotor between rotors-only and the complete vehicle is shown in Table 7. Lateral and longitudinal flapping angles are small, but their non-zero values prevent the flow on the rotor disk from being axisymmetric, as it would be expected for an isolated rotor in hover.

In the quadrotor, rotor-rotor and rotor-fuselage (if complete vehicle) interactions exist, changing the induced velocity and thus the rotor flows and airloads. This is reflected in Figure 11, where the $M^2 c_n$ aerodynamic loading distribution

(a) Rotor 1

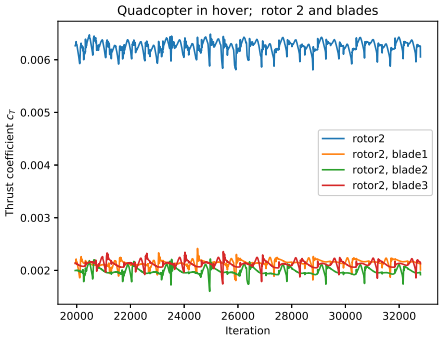

(b) Rotor 2

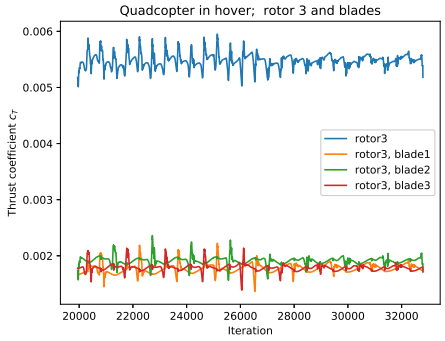

(c) Rotor 3

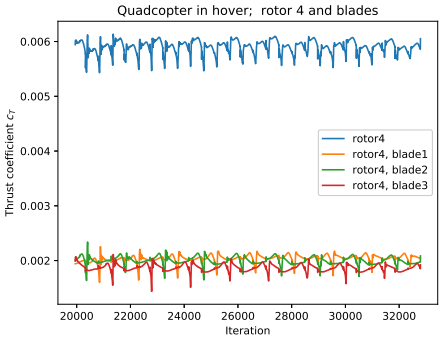

(d) Rotor 4

Fig. 8 Quadrotor thrust coefficient C_T in hover, as seen in OVERFLOW.

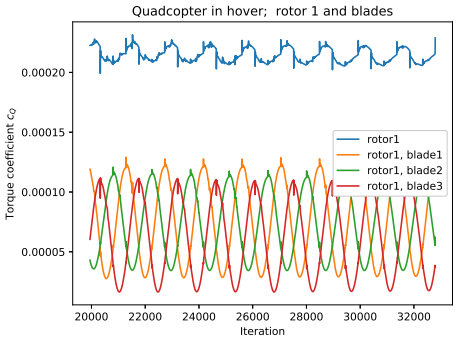

(a) Rotor 1

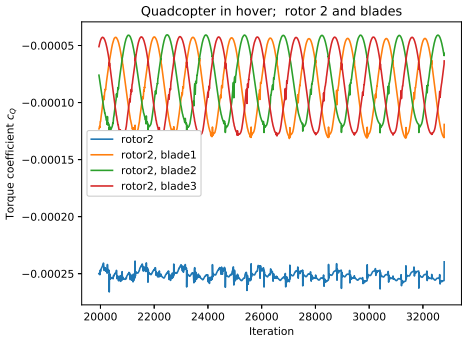

(b) Rotor 2

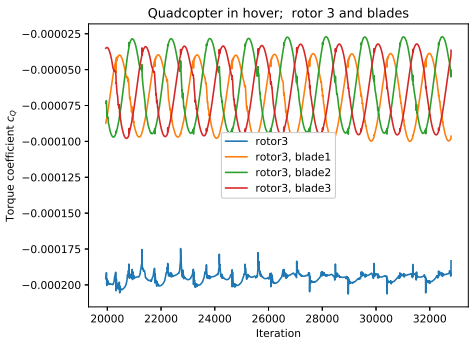

(c) Rotor 3

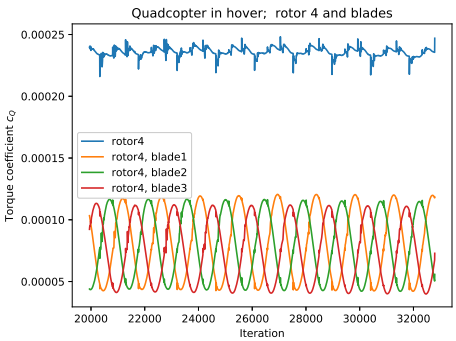

(d) Rotor 4

Fig. 9 Quadrotor torque coefficient C_Q in hover, as seen in OVERFLOW.

over the entire rotor disks is shown for the rotors-only and complete vehicle configurations. In this Figure, it can be observed that the flow is not axisymmetric, and this effect is stronger near the tip. In addition, symmetry among left and right rotors is no longer preserved in the case of the complete vehicle, as it can be observed on the trim angles and disk loading. The airframe has an effect on the final trim solution on the rotors, leading to differences between left and right rotors. The reason for this asymmetry may be due to the opposite direction of rotation and how the flow evolves differently downstream of the rotors.

The Q-criterion vorticity iso-surfaces colored with the vorticity magnitude for hover are shown in Figure 12. The wake geometry is complex and strong rotor-rotor interactions can be observed near the center for the rotors-only configuration (Fig. 12a. The airframe seems to partially block some interactions in the center region. Blade-vortex interactions (BVI) can be observed as well. BVI happens when the vortex shed by the previous blade impinges on the current blade, creating unsteady pressure fluctuations mainly near the leading edge. In the complete configuration, the airframe acts as a ground effect on the rotors, and that can increase rotor performance.

Figure 13 shows the vorticity contours on a vertical plane located at $y = 1.35R$. The vortex cores can be found by the red disks, and vortex sheets are observable where the light blue lines emerge from the wake core towards the vortex cores. In the case of rotors-only (Fig. 13a), rotor-rotor interactions lead to early vortex wake breakdown. When the airframe is added (Fig. 13b), a cleaner wake is found further downstream. Wake breakdown still happens in the inner wake near the airframe. In addition, the wake shape changes significantly with the airframe. Wake distorts more inward, closer to the vehicle.

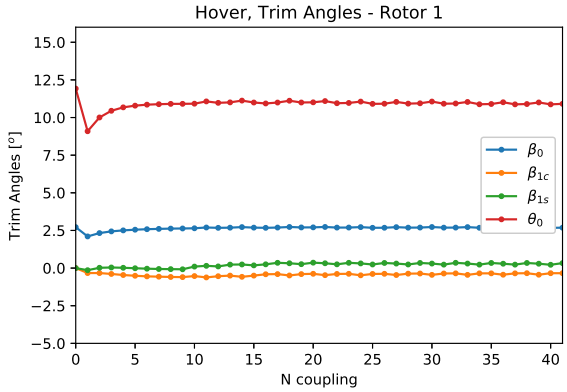

(a) Rotor 1 (front-right rotor) angles.

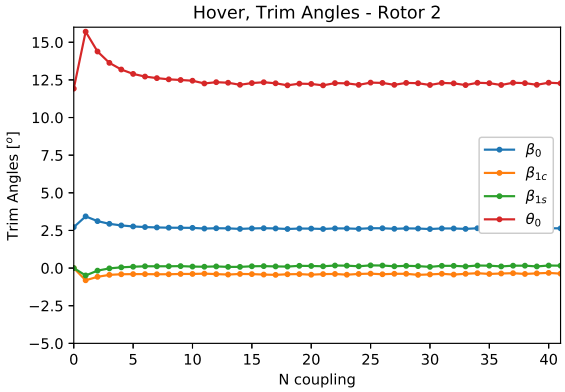

(b) Rotor 2 (front-left rotor) angles.

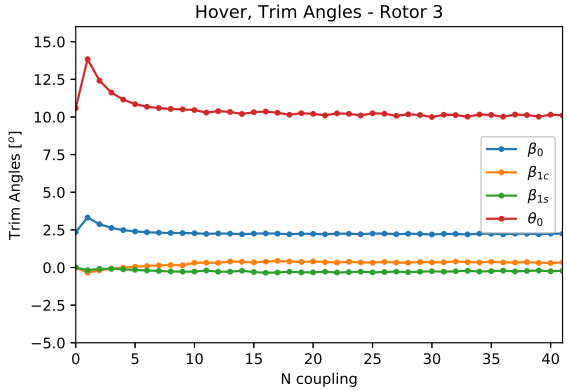

(c) Rotor 3 (rear-right rotor) trim angles.

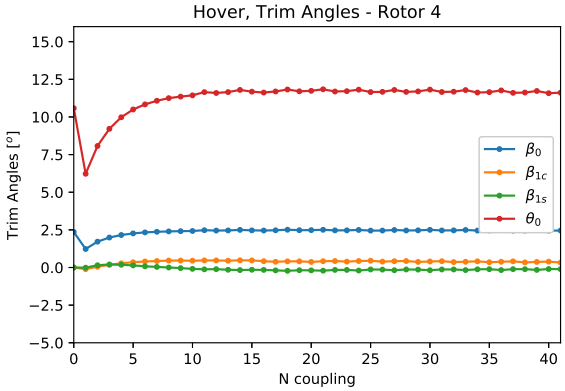

(d) Rotor 4 (rear-left rotor) trim angles.

Fig. 10 Quadrotor flapping and collective angles evolution with the number of loose-coupling iterations, in hover.

Table 8 shows a comparison of the aircraft figure of merit using CAMRAD II free wake, and OVERFLOW-CAMRAD II simulations. The predicted FM using the comprehensive analysis is higher than with high-fidelity

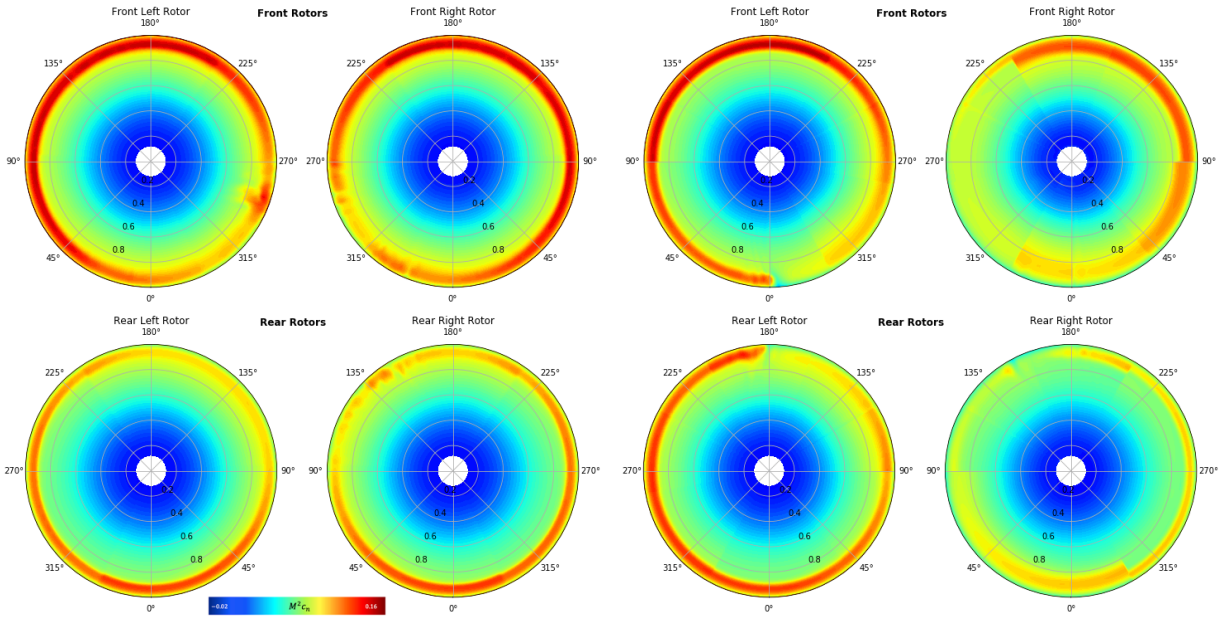

(a) Rotors-only (b) Complete vehicle

Fig. 11 Normal force M^2c_n on the rotor disk in hover. The rotor disks are seen from a plane above the quadrotor: the top-right disk corresponds to the front-right rotor (rotor 1), the top-left disk represents the front-left rotor (rotor 2), the bottom-right disk is the rear-right rotor (rotor 3), and the bottom-left disk is the rear-left rotor (rotor 4). Fig. 11a shows the normal force coefficient distribution for the rotors-only configuration and Fig. 11b shows the complete vehicle.

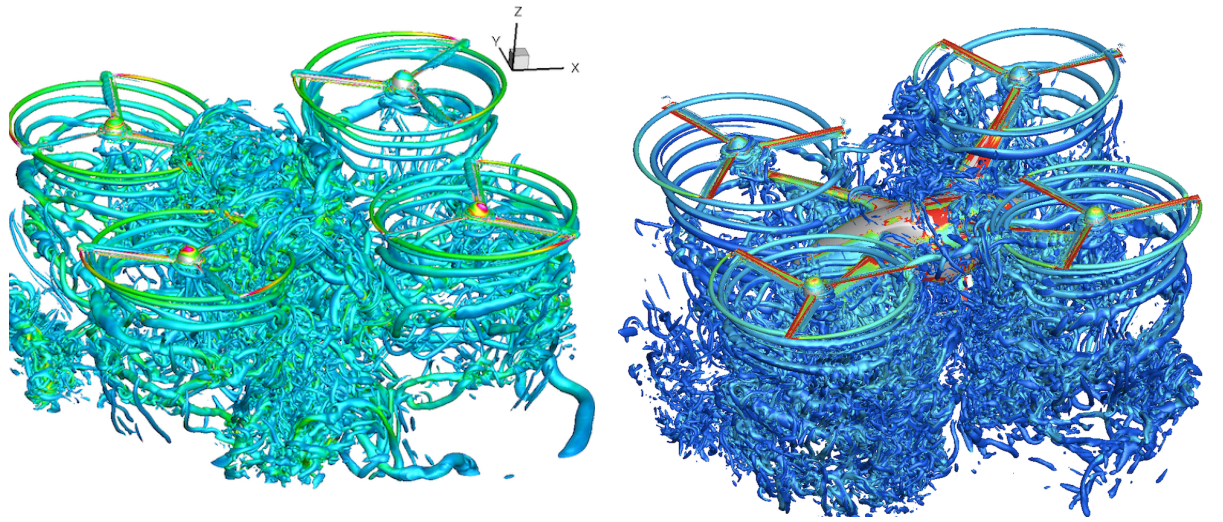

(a) Rotors-only (b) Complete vehicle

Fig. 12 Q-criterion vorticity iso-surfaces colored with the vorticity magnitude for the quadrotor in hover. Fig. 12a shows the rotors-only configuration and Fig. 12b shows the complete vehicle. The airframe blocks some rotor-rotor interactions.

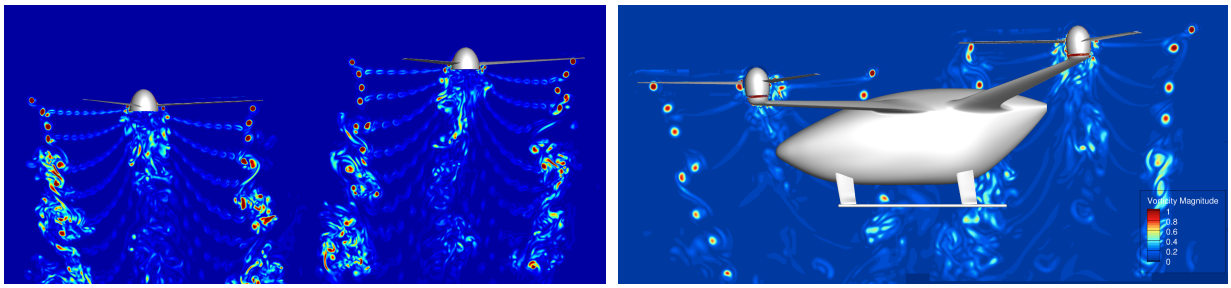

(a) Rotors-only **(b) Complete vehicle**

Fig. 13 Vorticity magnitude contours for the quadrotor in hover. Vortex sheets and vortex cores can be observed. Fig. 13a shows the rotors-only configuration and Fig. 13b shows the complete vehicle. Vortex wake breakdown happens early due to rotor-rotor interactions in Fig. 13a.

CFD tools. The complete vehicle FM predicted using OVERFLOW and CAMRAD II for trim is higher than for the rotors-only configuration. Although there is currently no experimental validation data for the conceptual designs, CAMRAD II, OVERFLOW, and our approach to model rotor flows have been validated in the past [9, 10, 12, 13, 15–17].

Table 8 Figure of Merit for the quadrotor.

Solver	Configuration	FM
CAMRAD II free wake	Complete	0.7986
OVERFLOW	Rotors-only	0.7105
OVERFLOW	Complete	0.7609

B. Cruise

Cruise simulations have been run with NASA's supercomputer using 2080 processors on Broadwell and Skylake nodes. Simulations run for 10 days and by the end of the simulation rotors rotated 32 revolutions. Cruise simulations generally converge faster than hover, therefore a higher rotor revolution count is reached for the same number of processors and running time and a similar number of grid points.

Figures 14 and 15 show the thrust and torque coefficients, C_T and C_Q, for quadrotor rotors in cruise. The solution is periodic for each blade, and higher variations than in hover between the maximum and minimum values can be observed.

Table 9 shows the final coning, flapping, and collective angles for the trimmed solution in cruise. The rotors-only and complete vehicle solutions are compared. Differences between left and right rotors are smaller for the rotors-only than for the complete vehicle. Nevertheless, the asymmetry in cruise is relatively smaller than in hover. The explanation where the airframe may affect the trim solution seems consistent with these results, as weaker interactions with the airframe are to be expected in cruise.

Table 9 Final angles for the quadrotor rotors-only and complete vehicle configurations, in cruise conditions.

Configuration	Rotors-only				Complete Vehicle			
Rotor # / Angles	β_0 [^{o}]	β_{1c} [^{o}]	β_{1s} [^{o}]	θ_0 [^{o}]	β_0 [^{o}]	β_{1c} [^{o}]	β_{1s} [^{o}]	θ_0 [^{o}]
Rotor 1	2.46	-5.13	3.97	15.77	2.35	-4.75	3.8	15.10
Rotor 2	2.44	-5.15	3.97	15.73	2.46	-5.21	3.84	15.68
Rotor 3	2.56	-5.41	4.26	16.49	2.57	-5.32	4.59	16.34
Rotor 4	2.58	-5.41	4.25	16.52	2.53	-5.34	4.58	16.49

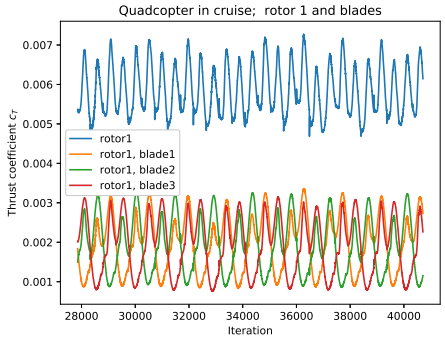

(a) Rotor 1

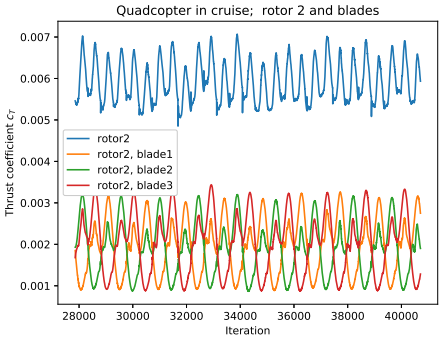

(b) Rotor 2

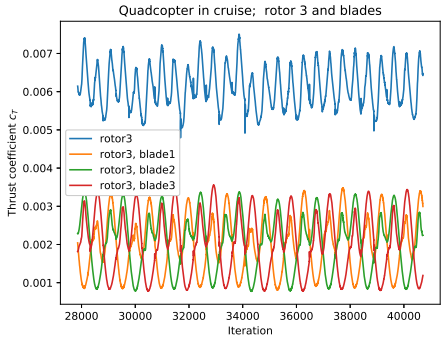

(c) Rotor 3

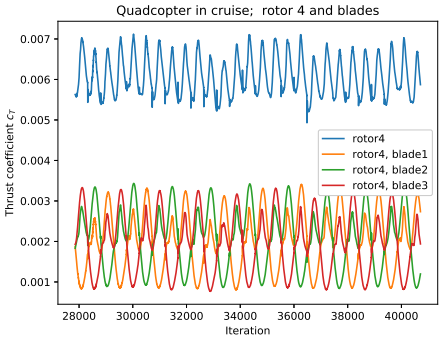

(d) Rotor 4

Fig. 14 Quadrotor thrust coefficient C_T in cruise, as seen in OVERFLOW.

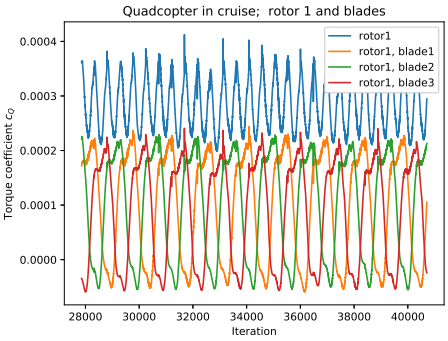

(a) Rotor 1

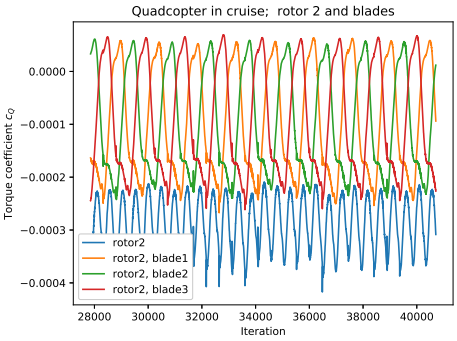

(b) Rotor 2

(c) Rotor 3

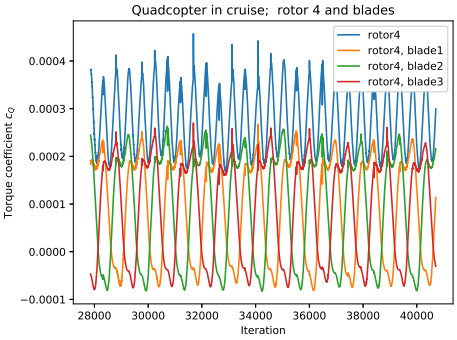

(d) Rotor 4

Fig. 15 Quadrotor torque coefficient C_Q in cruise, as seen in OVERFLOW.

Figure 16 shows the predicted normal loading M^2c_n for the two configurations. Similar aerodynamic loadings between rotors and configurations can be observed. The rear rotors are placed high enough and far from the front rotor wakes than rotor-rotor interactions do not significantly affect rear rotor performance. The main BVI event can be observed on the advancing side. Precisely, BVI is located at the second quadrant of each disk ($90^o < \psi < 180^o$), at approximately $r = 0.65R$, and it is shown as the thin red arc. In edgewise flight, BVI causes a high amplitude impulse, being one of the main sources of noise. It also affects the loading on the blade, mostly on the leading edge region. On the retreating side ($180^o < \psi < 360^o$), there exists a small region of reversed flow*. This affects the disk loading, where the normal force coefficient is zero or negative.

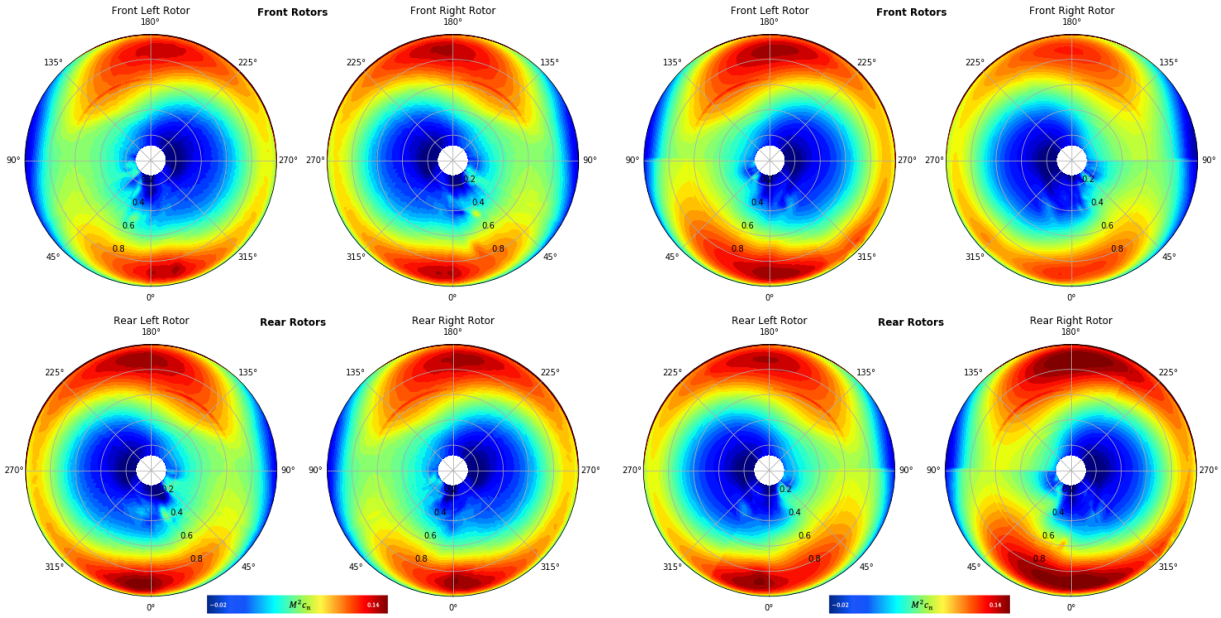

(a) Rotors-only **(b) Complete vehicle**

Fig. 16 Normal force M^2c_n on the rotor disk in cruise. The rotor disks are seen from a plane above the quadrotor: the top-right disk corresponds to the front-right rotor, the top-left disk represents the front-left rotor, the bottom-right disk is the rear-right rotor, and the bottom-left disk is the rear-left rotor. Fig. 16a shows the normal force coefficient distribution for the rotors-only configuration and Fig. 16b shows the complete vehicle.

Figure 17 shows the Q-criterion vorticity iso-surfaces colored with the vorticity magnitude. Higher vorticities are found near the vortex cores or where the flow is separated. Elevating the rear rotors above the front rotors reduces the rotor-rotor interactions by reducing the interference among the wakes. The BVI can be clearly seen when looking at the front-right rotor (rotor 1) in Figure 17a. The vortex shed from the previous blade ($\psi = 240^o$) impinges on the current blade ($\psi = 120^o$). A supertip vortex develops out of the front rotors wake for the complete vehicle (Figure 17b). There is separated flow from the hubs and fuselage. The vortex sheets can be seen in Figure 17b for the rear rotors. It is more clearly observed for rotor 4, blade at $\psi = 330^o$. These images reveal the complex flows present in multi-rotor vehicles.

Figure 18 shows the vorticity contours on a vertical plane by the right rotors ($y = 1.35R$). This image clearly shows that the wakes from the front rotors do not interact directly with the rear rotors. The tip vortices can be found by the small red disks. Separated flow from the hubs is the main flow feature seen in the images. The addition of the airframe limits the upward movement of the wake from the front rotors and vortex wakes are closer in the rotors-only configuration. As a result, rotor-rotor interactions are further decreased.

Table 10 shows a comparison of the aircraft lift-to-drag ratio for each analysis performed in this work. First, the free wake CAMRAD II analysis gives a $L/D_e = 5.135$. The L/D_e from the OVERFLOW simulations is calculated in CAMRAD II using the aerodynamics loads from CFD, which is $\approx 35\%$ lower. This effect on L/D_e has been previously observed in [5, 6] and remains an open subject for further investigation.

*The locus of this region can be found where the in-plane component of the local flow velocity is zero, that is $0 = \Omega R(r + \mu \sin\psi)$. The reverse flow region has a diameter of μ, and with increasing advance ratios, the size of the reverse flow region increases.

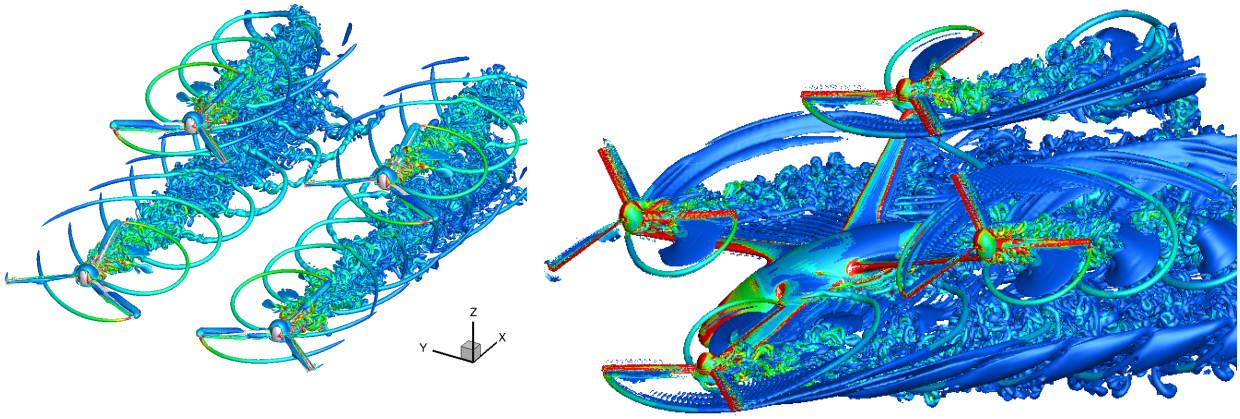

(a) Rotors-only **(b) Complete vehicle**

Fig. 17 Q-criterion vorticity iso-surfaces colored with the vorticity magnitude for the quadrotor in cruise.

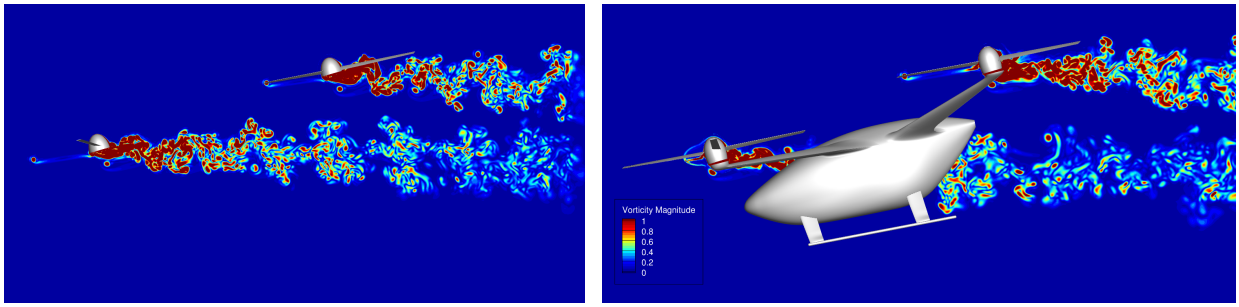

(a) Rotors-only **(b) Complete vehicle**

Fig. 18 Vorticity magnitude contours for the quadrotor in cruise, for the rotors-only (Fig. 18a) and the complete vehicle (Fig. 18b). The rotor vortex wakes can be observed.

Table 10 Aircraft effective lift-to-drag ratio.

Solver	Configuration	Aircraft L/D_e
CAMRAD II free wake	Complete	5.135
OVERFLOW	Rotors-only	3.288
OVERFLOW	Complete	3.309

V. Summary

NASA's quadrotor air taxi concept for urban air mobility has been studied in this work using rotorcraft comprehensive analysis tools and high-fidelity CFD.

The comprehensive code CAMRAD II has first been used to perform an analysis using free wake. The wake geometry, trim angles, and performance in hover and in cruise have been obtained.

Then, CAMRAD II has been loosely coupled with OVERFLOW. High-fidelity CFD simulations have been carried out on overset grids for the complete quadrotor, and the results have been compared with the rotors-only configuration, which consists of only the rotors and hubs, removing all other vehicle components. The rotor angles and motions, and the aircraft trim are predicted by CAMRAD II. The thrust and torque coefficients, airloads, final angles, wake geometries, and performance have been analyzed.

The complete vehicle performed better overall than the rotors-only configuration. Figure of merit and aircraft efficiency in edgewise flight have been obtained. The comparison with free wake yield lower values, a phenomenon that has been observed in previous studies.

Rotor wake geometry revealed the positive effect of adding the airframe by decreasing rotor-rotor interactions in hover. In cruise, the visualization of the wake showed that the placement of the rear rotors is high enough that rotor-rotor interactions with the front rotors are minimum. Aerodynamic interactions have a significant impact on performance, noise, and vibrations. The interactions strongly depend on the positioning of the rotors. Elevating the rear rotors above the front rotors reduces the rotor-rotor interactions by reducing the interference among the wakes.

NASA's quadcopter air taxi concept is one of the concept vehicles expected to focus and guide NASA's research activities in support of aircraft development for emerging aviation markets, in particular VTOL air taxi operations.

VI. Acknowledgements

This work is supported by the Revolutionary Vertical Lift Technology (RVLT) Project (PM: Susan Gorton; PI: Brian Allan). The computations utilized the Pleiades, Electra, and Aitken supercomputers at the NASA Advanced Supercomputing Division. The authors would like to thank Wayne Johnson, Chris Silva, Gloria Yamauchi, and Brian Allan for helpful discussions. David Garcia helped with the review of this manuscript.

References

[1] Johnson, W., and Silva, C., "NASA concept vehicles and the engineering of advanced air mobility aircraft," *The Aeronautical Journal*, October 2021, pp. 1–33. https://doi.org/10.1017/aer.2021.92.

[2] Johnson, W., and Silva, C., "Observations from Exploration of VTOL Urban Air Mobility Designs," *The Asian/Australian Rotorcraft Forum*, October 2018.

[3] Ventura Diaz, P., and Yoon, S., "Computational Study of NASA's Quadrotor Air Taxi Concept," *AIAA Paper 2020–0302*, January 2020. https://doi.org/10.2514/6.2020-0302.

[4] Ventura Diaz, P., and Yoon, S., "High-Fidelity Computational Aerodynamics of Multi-Rotor Unmanned Aerial Vehicles," *AIAA Paper 2018–1266*, January 2018. https://doi.org/10.2514/6.2018-1266.

[5] Ventura Diaz, P., Johnson, W., Ahmad, J., and Yoon, S., "Computational Study of the Side-by-side Urban Air Taxi Concept," *VFS 75th Forum*, May 2019.

[6] Ventura Diaz, P., Johnson, W., Ahmad, J., and Yoon, S., "The Side-by-side Urban Air Taxi Concept," *AIAA Paper 2019–2828*, June 2019. https://doi.org/10.2514/6.2019-2828.

[7] Ventura Diaz, P., Caracuel, R., and Yoon, S., "Simulations of Ducted and Coaxial Rotors for Air Taxi Operations," *AIAA Paper 2019–2825*, June 2019. https://doi.org/10.2514/6.2019-2825.

[8] Ventura Diaz, P., and Yoon, S., "A Physics-Based Approach to Urban Air Mobility," *European Rotorcraft Forum, Paper 18*, September 2018.

[9] Yoon, S., Ventura Diaz, P., Boyd, D. D., Chan, W. M., and Theodore, C. R., "Computational Aerodynamic Modeling of Small Quadcopter Vehicles," *AHS Paper 73-2017-0015*, May 2017.

[10] Pulliam, T. H., "High Order Accurate Finite-Difference Methods: as seen in OVERFLOW," *AIAA Paper 2011–3851*, June 2011. https://doi.org/10.2514/6.2011-3851.

[11] Chan, W. M., Gomez, R. J., Rogers, S. E., and Buning, P. G., "Best Practices in Overset Grid Generation," *AIAA Paper 2002–3191*, June 2002. https://doi.org/10.2514/6.2002-3191.

[12] Johnson, W., "Rotorcraft Aerodynamic Models for a Comprehensive Analysis," *American Helicopter Society 54th Annual Forum*, May 1998.

[13] Potsdam, M., Yeo, H., and Johnson, W., "Rotor Airloads Prediction Using Loose Aerodynamics/Structural Coupling," *Journal of Aircraft*, Vol. 43, No. 3, 2006, pp. 732–742. https://doi.org/10.2514/1.14006.

[14] Haimes, R., and Dannenhoffer, J., "The Engineering Sketch Pad: A Solid-Modeling, Feature-Based, Web-Enabled System for Building Parametric Geometry," *AIAA Paper 2013–3073*, June 2013. https://doi.org/10.2514/6.2013-3073.

[15] Yoon, S., Chaderjian, N. M., Pulliam, T. H., and Holst, T. L., "Effect of Turbulence Modeling on Hovering Rotor Flows," *AIAA Paper 2015–2766*, June 2015. https://doi.org/10.2514/6.2015-2766.

[16] Yoon, S., Lee, H. C., and Pulliam, T. H., "Computational Analysis of Multi-Rotor Flows," *AIAA Paper 2016–0812*, January 2016. https://doi.org/10.2514/6.2016-0812.

[17] Yoon, S., Lee, H. C., and Pulliam, T. H., "Computational Study of Flow Interactions in Coaxial Rotors," *AHS Technical Meeting on Aeromechanics Design for Vertical Lift*, January 2016.

[18] Spalart, P., Jou, W.-H., Strelets, M., and Allmaras, S., "Comments on the Feasibility of LES for Wings, and on a Hybrid RANS/LES Approach," *Advances in DNS/LES, Greyden Press*, 1997, pp. 137–147.

[19] Spalart, P. R., "Strategies for Turbulence Modeling and Simulations," *International Journal of Heat and Fluid Flow*, Vol. 21, No. 3, 2000, pp. 252–263. https://doi.org/10.1016/S0142-727X(00)00007-2.

[20] Johnson, W., "Technology Drivers in the Development of CAMRAD II," *American Helicopter Society Aeromechanics Specialist Meeting*, January 1994.

[21] Johnson, W., "A General Free Wake Geometry Calculation for Wings and Rotors," *American Helicopter Society 51st Annual Forum*, May 1995.